Random lattice deformations in rare-earth-doped cubic hexafluoroelpasolites: High-resolution optical spectroscopy and theoretical studies

B. Z. Malkin,[1] D. S. Pytalev,[2,*] M. N. Popova,[2] E. I. Baibekov,[1] M. L. Falin,[1,3] K. I. Gerasimov,[1,3] and N. M. Khaidukov[4]

[1]*Kazan (Volga Region) Federal University, Kazan 420008, Russian Federation*

[2]*Institute of Spectroscopy RAS, Troitsk, Moscow 142190, Russian Federation*

[3]*Kazan Physical–Technical Institute RAS, Kazan 420029, Russian Federation*

[4]*Institute of General and Inorganic Chemistry RAS, Moscow 119991, Russian Federation*

(Received 11 July 2012; revised manuscript received 14 September 2012; published 11 October 2012)

High-resolution Fourier spectroscopy is used to study the low-temperature (3–10 K) optical absorption spectra of Cs_2NaYF_6 and Cs_2NaScF_6 crystals doped with rare-earth ions, which substitute for Y^{3+} or Sc^{3+} ions at sites with cubic O_h symmetry. Splitting of some absorption lines corresponding to doublet (Γ_6 or Γ_7)–quadruplet (Γ_8) transitions in the Kramers Yb^{3+}, Er^{3+}, and Sm^{3+} ions and a singlet (Γ_1)–triplet (Γ_4) transition in the non-Kramers Tm^{3+} ion is observed. In the vicinity of these lines, additional spectral satellites with intensities depending nonlinearly on the concentration of the rare-earth ions are present. We argue that the observed splitting is caused by low-symmetry components of the crystal field induced by random lattice strains. An explicit expression for the generalized distribution function of local strains produced by random point defects in the elastic continuum is derived and used to simulate the line shapes. A satisfactorily agreement with the measured spectra is achieved. The observed satellite transitions are ascribed to pairs of the nearest-neighbor rare-earth ions interacting through the dynamic lattice deformations.

DOI: 10.1103/PhysRevB.86.134110 PACS number(s): 61.72.Bb, 78.40.−q, 71.70.Ch

I. INTRODUCTION

Zero-phonon optical intraconfiguration $4f$-$4f$ transitions of rare-earth (R) ions in real crystals are always inhomogeneously broadened. Sometimes, a fine structure of a spectral line can be resolved. It may originate from an isotopic disorder[1–4] or hyperfine interactions.[5] When an optical transition involves at least one degenerate electronic energy level, the resolved fine structure can be a result of random lattice strains.[4] The observed spectral profile is characterized by the specific distribution of intervals and intensities of individual components of the structure. A theoretical analysis of the measured fine structure can provide information about random perturbations of the crystal lattice, as recently demonstrated in Ref. 4 on the example of the spectra of a non-Kramers ion Tm^{3+} residing in the S_4 point symmetry positions of the $LiYF_4$ crystal lattice. As for Kramers ions (i.e., ions with an odd number of electrons), all degeneracy except the twofold Kramers one is lifted for site symmetries lower than the cubic one. Thus, only in a cubic environment, where their energy spectrum contains fourfold degenerate levels, Kramers R ions can serve as probes of lattice strains. For non-Kramers R ions, two- and threefold degenerate energy levels are present in the case of a cubic environment, which also gives a possibility to probe random lattice strains. To our knowledge, the influence of random lattice strains on the spectra of the R ions residing at sites of a cubic symmetry has not been previously studied.

In the present work, we measured high-resolution absorption spectra of R-doped cubic fluoride crystals Cs_2NaYF_6 and Cs_2NaScF_6 with the elpasolite structure $Fm3m$. In these crystals, impurity R ions substitute for Y^{3+} or Sc^{3+} at sites with point O_h symmetry (the first coordination shell is the fluorine octahedron). Optical spectra of Cs_2NaYF_6 and Cs_2NaScF_6 crystals doped with samarium, erbium, thulium, and ytterbium, as well as spectra of stoichiometric elpasolites Cs_2NaErF_6, Cs_2NaTmF_6, and Cs_2NaYbF_6, in the infrared, visible, and ultraviolet regions were studied in Refs. 6–13. However, the previously measured spectra were taken with resolution not high enough to detect small splitting of spectral lines induced by random low-symmetry components of the crystal fields, by hyperfine interactions, or both. Accordingly, we decided to perform high-resolution spectral measurements with the aims to register true profiles of the spectral lines and to study quantitatively the dependence of lattice strains in cubic crystals on the type and concentration of impurity ions by comparisons between the simulated spectra and the experimental data.

This paper begins with a description of the measured spectral lines demonstrating a pronounced fine structure (Sec. II). Section III A puts forward a model to calculate the spectral envelopes, generated by lattice strains in a cubic crystal, for transitions involving degenerate crystal-field levels. A possible contribution of the hyperfine interactions is analyzed in Sec. III B, which shows that the hyperfine structure of transitions in the odd R isotopes cannot be responsible for the observed spectral profiles. At the next step of the theoretical analysis, a generalized distribution function of lattice strains is derived (Sec. III C), electron–deformation coupling constants are estimated (Sec. III D), and lattice strains in Cs_2NaYF_6 and Cs_2NaScF_6 crystals with different concentrations of impurity R ions are characterized (Sec. III E). A semiphenomenological model of satellites in the spectra of samples containing enlarged concentrations of the Yb^{3+} and Er^{3+} ions is proposed at the end of this last section. Section IV summarizes the main results and conclusions.

II. EXPERIMENTAL RESULTS

Crystals of cubic elpasolites Cs_2NaYF_6 and Cs_2NaScF_6 doped with optically active R ions were grown under hydrothermal conditions. For hydrothermal experiments, copper-insert lined autoclaves with a volume of ∼40 cm^3 were utilized,

TABLE I. Parameter values used in simulations of the absorption line shapes in fluoroelpasolites (column 1) with different concentrations (column 2) of R ions. Crystal-field parameters are given in columns 3 and 4. Columns 6 and 7 contain effective constants of interaction with the Γ_{3g} and Γ_{5g} strains, respectively, for the degenerate final (initial for Er^{3+}) level (column 5) of an optical transition. Widths of the strain distribution and the line form function are in columns 8 and 9, respectively.

	c (at.%)	B_4 (cm^{-1})	B_6 (cm^{-1})	Degenerate level	$v(\Gamma_{3g})$ (cm^{-1})	$v(\Gamma_{5g})$ (cm^{-1})	γ (10^{-5})	Δ (cm^{-1})
1	2	3	4	5	6	7	8	9
$Cs_2NaYF_6:Yb^{3+}$	0.01	313	−8.5	$\Gamma_8(^2F_{5/2})$	6665	876	3.2	0.0025
	1						4.1	
$Cs_2NaScF_6:Yb^{3+}$	0.1	314	−7.5	$\Gamma_8(^2F_{5/2})$	6665	876	5.3	0.0025
	2						29	
$Cs_2NaYF_6:Tm^{3+}$	0.1	321.4	16.6	$\Gamma_4(^3H_5)$	953	536	6	0.0050
	1						15	
$Cs_2NaYF_6:Er^{3+}$	0.3	337	18.4	$\Gamma_8(^4I_{15/2})$	311	188	3.2	0.0096
$Cs_2NaYF_6:Sm^{3+}$	3	409	21.9	$\Gamma_8(^6H_{13/2})$	57	560	28	0.0450

and the inserts were separated by perforated diaphragms into synthesis and crystallization zones. The fluoride crystals were synthesized by a direct temperature-gradient method as a result of the reaction of the aqueous solutions containing 35–40 mol.% CsF and 8–10 mol.% NaF with oxide mixtures $(1-x)Y_2O_3 - xLn_2O_3$ or $(1-x)Sc_2O_3 - xYb_2O_3$ at a temperature of ∼750 K in the synthesis zone, a temperature gradient along the reactor body of up to 3 K/cm, and a pressure of ∼100 MPa. Under these conditions, spontaneously nucleated crystals of up to 0.5 cm^3 were grown in the upper crystallization zone of the autoclave for 200 h. The purities of the utilized oxides were 99.99% for R oxides and 99.9% for Sc_2O_3. Nominal concentrations of impurity R ions in the studied crystals are given in Table I.

Absorption spectra were measured in a broad spectral range from 5000 to 23 000 cm^{-1} at a resolution up to 0.01 cm^{-1} using an infrared Fourier spectrometer Bruker IFS 125 and a closed-cycle cryostat Cryomech ST 403 at temperatures from 3 to 10 K. At these temperatures, the recorded spectral lines correspond to transitions taking their origin from the lowest crystal-field sublevel of the ground multiplet, i.e., $\Gamma_6(^2F_{7/2})$ of Yb^{3+}, $\Gamma_8(^4I_{15/2})$ of Er^{3+}, $\Gamma_7(^6H_{5/2})$ of Sm^{3+}, or $\Gamma_1(^3H_6)$ of Tm^{3+} (Γ_i is the corresponding irreducible representation of the O_h point symmetry group), separated by a rather large gap Λ from the first excited sublevel (in particular, $\Lambda = 327$, 286, and 113 cm^{-1} for the Yb^{3+},[11] Sm^{3+},[12] and Tm^{3+}[6] impurity ions, respectively, in Cs_2NaYF_6 and 65 cm^{-1} for the Er^{3+} ions in Cs_2NaErF_6[10]).

In crystals with a low concentration c of impurity ions ($c \leqslant 0.1$ at.%), the absorption lines correspond to transitions in isolated optical centers. For several transitions between the doublet (Γ_6 or Γ_7) and the quadruplet (Γ_8) states of the Kramers ions Yb^{3+}, Sm^{3+}, and Er^{3+}, a specific narrow dip is observed at the center of the line when the upper state of a transition is the lowest crystal-field sublevel of an excited multiplet (the phonon broadening is not effective for these sublevels at low temperatures, and correspondingly, they have minimal widths). In particular, the doublet structure of such a type is observed for the transitions $\Gamma_6(^2F_{7/2}) \rightarrow \Gamma_8(^2F_{5/2})$ in Yb^{3+} (Figs. 1 and 2), $\Gamma_8(^4I_{15/2}) \rightarrow \Gamma_6(^4I_{13/2})$ in Er^{3+} [Fig. 3(a)] and $\Gamma_7(^6H_{5/2}) \rightarrow \Gamma_8(^6H_{13/2})$ in Sm^{3+} [Fig. 3(b)]. More complicated structure is observed for the transition between the singlet ground state $\Gamma_1(^3H_6)$ and the excited triplet $\Gamma_4(^3H_5)$ in the absorption spectra of the non-Kramers Tm^{3+} ions (Fig. 4), where the corresponding spectral line is split into three components. It is worth noting that the experimental doublet line profiles cannot be represented by a sum of separate lines with symmetric line shapes.

The widths of the dips (the difference $\Delta\varepsilon$ between the transition energies corresponding to peaks in the split line), as well as the widths of the components of the split lines, increase with increasing concentration of the impurity ions. The measured values of $\Delta\varepsilon$ are in the range from 0.03 to 2.6 cm^{-1} and are comparable to or substantially larger than any hyperfine splitting that we might expect for the degenerate

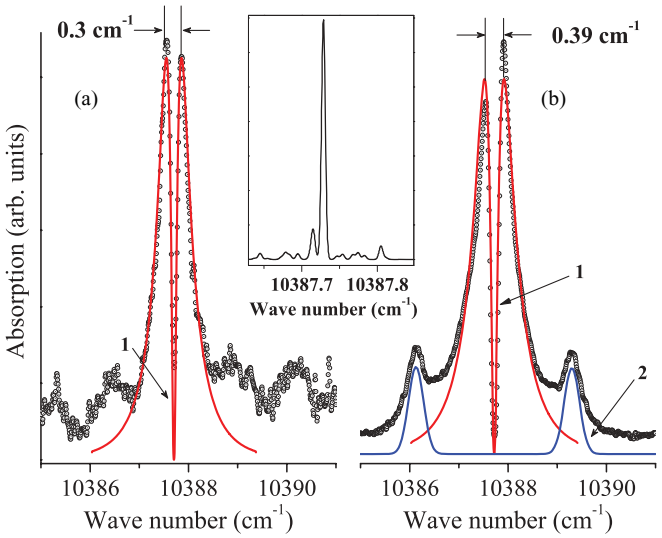

FIG. 1. (Color online) Measured (symbols) and simulated (solid curves 1 and 2 corresponding to single ion and dimer centers, respectively) absorption line shapes for the transition $^2F_{7/2}(\Gamma_6) \rightarrow {}^2F_{5/2}(\Gamma_8)$ in $Cs_2NaYF_6:Yb^{3+}$ samples with the ytterbium concentrations (a) 0.01 at.% and (b) 1 at.%. Spectra were taken with the resolutions 0.05 and 0.1 cm^{-1}, respectively, at temperature $T = 3.5$ K. The inset shows the spectral envelope calculated for a perfect sample (without random strains) containing odd and even Yb isotopes with natural abundances.

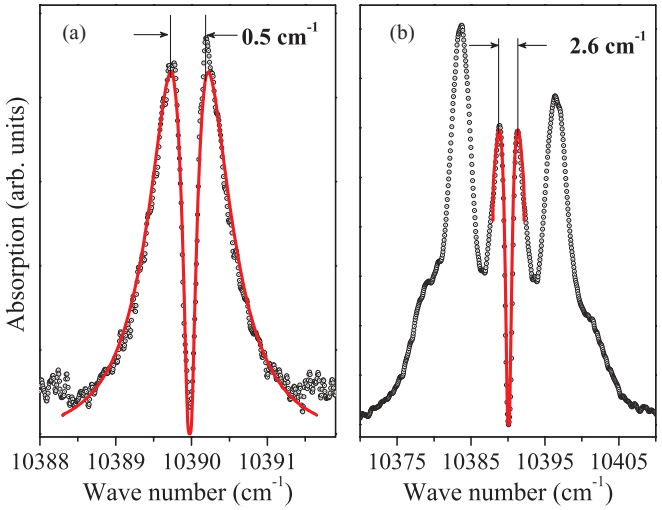

FIG. 2. (Color online) Measured (symbols) and simulated (solid curves) absorption line shapes for the transition ${}^2F_{7/2}(\Gamma_6) \rightarrow {}^2F_{5/2}(\Gamma_8)$ in Cs_2NaScF_6:Yb^{3+} with the ytterbium concentrations (a) 0.1 at.% with spectral resolution 0.05 cm^{-1} and (b) 2 at.% with spectral resolution 0.1 cm^{-1}. $T = 3.5$ K. Wave number scales in (a) and (b) differ by an order of magnitude.

crystal-field sublevels of the odd R isotopes ${}^{173}Yb^{3+}$, ${}^{171}Yb^{3+}$, ${}^{169}Tm^{3+}$, ${}^{167}Er^{3+}$, ${}^{149}Sm^{3+}$, and ${}^{147}Sm^{3+}$ (a more detailed comparison is presented later).

Additional satellites of the transition $\Gamma_6({}^2F_{7/2}) \rightarrow \Gamma_8({}^2F_{5/2})$ are observed in the spectra of the yttrium and scandium elpasolites containing Yb^{3+} ions with concentrations larger than 0.1 at.% [Figs. 1(b) and 2(b)]. Intensities of these

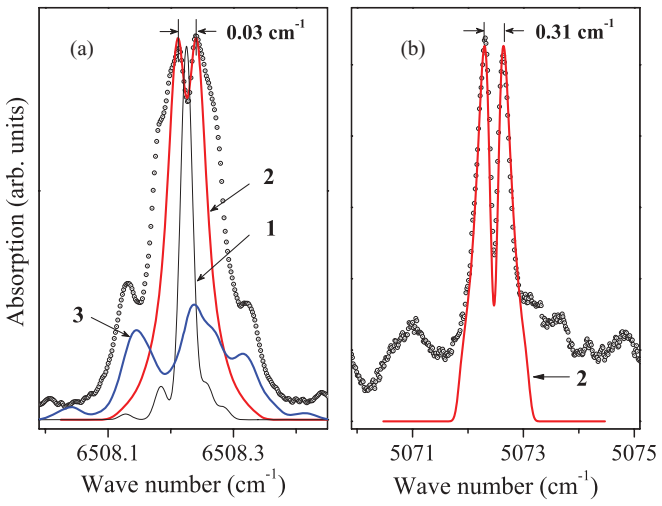

FIG. 3. (Color online) Measured (symbols) absorption line shapes for (a) the transition ${}^4I_{15/2}(\Gamma_8) \rightarrow {}^4I_{13/2}(\Gamma_6)$ in Cs_2NaYF_6:Er^{3+} (0.3 at.%) at $T = 4$ K, and (b) the transition ${}^6H_{5/2}(\Gamma_7) \rightarrow {}^6H_{13/2}(\Gamma_8)$ in Cs_2NaYF_6:Sm^{3+} (3 at.%) at $T = 5$ K. The results of simulations are represented by solid curves: curve 1, the sum of spectral envelopes for even and odd erbium isotopes with natural abundances in the perfect cubic lattice; curve 2, spectral envelopes for single ions of even isotopes with the doublet structure caused by random strains; and curve 3, the spectral envelope for the erbium dimer. Wave number scales in (a) and (b) differ by an order of magnitude.

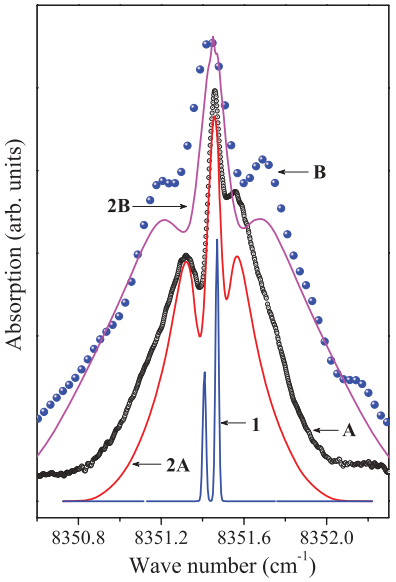

FIG. 4. (Color online) Measured (symbols) and simulated (solid curves) absorption line shapes for the transition ${}^3H_6(\Gamma_1) \rightarrow {}^3H_5(\Gamma_4)$ in Cs_2NaYF_6:Tm^{3+} (data A for $c = 0.1$ at.%, $T = 4$ K, and data B for $c = 1$ at.%, $T = 5$ K). Curve 1 represents the simulated line in the perfect lattice; curves 2A and 2B were computed with taking into account the random strains.

satellites, which are shifted symmetrically from the line center by ± 1.6 and ± 3.7 cm^{-1} in Cs_2NaYF_6:Yb (1 at.%) and by ± 6.5 and ± 10.5 cm^{-1} in Cs_2NaScF_6:Yb (2 at.%), increase nonlinearly with the concentration of the Yb^{3+} ions. The satellites with much smaller shifts of about ± 0.1 cm^{-1} also are observed for the $\Gamma_8({}^4I_{15/2}) \rightarrow \Gamma_6({}^4I_{13/2})$ transition in the Er^{3+} ions [Fig. 3(a)].

The observed fine structures of the spectral lines corresponding to transitions that involve degenerate crystal-field levels of different R ions give evidence for low-symmetry local perturbations, which can be related to random electric multipole fields. In general, low-symmetry components of the crystal field affecting a R ion can be induced by native crystal lattice point defects. Isotopic disorder is absent in the host crystal lattices studied in the present work. However, impurity R ions also perturb the local crystal lattice structure and induce random strains when substituting for ions with different ionic radii.

The satellites of spectral lines with concentration-dependent relative intensities are evidently induced by interactions between the R ions. The well-resolved satellites for zero-phonon optical transitions involving the Γ_8 crystal-field levels also were observed earlier in $Cs_2NaErCl_6$, $Cs_2NaYbCl_6$, and Cs_2NaYbF_6 crystals[14] at rather large distances, up to 10 cm^{-1}, from the central line. The magnetic origin of the satellites proposed in Ref. 14 seems to be excluded, because the magnetic ordering temperatures of R hexafluoroelpasolites are less than 0.1 K.[15] The observed spectral lines corresponding to transitions between Kramers doublets do not have satellites. We argue that electric multipolar interactions between the R ions mediated by local static and dynamic lattice deformations play the dominant role in the formation of satellites of

the $\Gamma_8 \leftrightarrow \Gamma_6,\Gamma_7,\Gamma_8$ transitions observed in elpasolite-type crystals containing high concentrations of the R ions.

In the following sections, the simulations of the spectral envelopes are presented for the R ions interacting with random strains induced by point lattice defects in hexafluoroelpasolites. Among the conventional mechanisms giving the inhomogeneous broadening of spectral lines in solids,[16] this is the one that is consistent with the observed fine structure of the doublet–quadruplet transitions. Calculations reproduce well the results of measurements.

III. MODELING OF THE LINE SHAPES

A. Spectral envelope

The Hamiltonian of a R ion in a dielectric crystal operating in the space of states of the electronic $4f^N$ configuration is written as follows:

$$H = H_0 + H_{\rm CF} + H_{\rm e-ph} + H_{\rm ed}(\boldsymbol{e}). \tag{1}$$

Here, H_0 is the energy of a free ion, $H_{\rm CF}$ is the energy of $4f$ electrons in the static crystal field in the perfect crystal lattice, $H_{\rm e-ph}$ is the Hamiltonian of the electron–phonon interaction, and $H_{\rm ed}$ stands for changes of the crystal-field energy due to lattice strains determined by the deformation tensor $\boldsymbol{e}$. A standard parameterized form of H_0 that involves electrostatic, spin–orbit, configuration and correlated spin–orbit and spin–spin interactions is used here.[17] The crystal-field Hamiltonian of the R ions in hexafluoroelpasolites written in the crystallographic system of coordinates (when the z-axis is parallel to the C_4 symmetry axis) contains only two parameters, B_4 and B_6, and has the following form:

$$H_{\rm CF} = B_4\big(O_4^0 + 5O_4^4\big) + B_6\big(O_6^0 - 21O_6^4\big). \tag{2}$$

Here, operators O_p^k ($|k| \leqslant p$) are linear combinations of spherical tensor operators $C_k^{(p)}$; the explicit relations between operators O_p^k and $C_k^{(p)}$ are presented in Ref. 18. In the case of $(2J+1)$ states belonging to a multiplet with the total angular momentum J, the operators O_p^k coincide with Stevens' operators[19] multiplied by the corresponding reduced matrix elements.

Components of the deformation tensor for a cubic crystal transform according to the Γ_{1g}, Γ_{3g}, and Γ_{5g} irreducible representations of the O_h group: $e(\Gamma_{1g}) = (e_{xx}+e_{yy}+e_{zz})/3$; $e_1(\Gamma_{3g}) = (2e_{zz}-e_{xx}-e_{yy})/2\sqrt{3}$ and $e_2(\Gamma_{3g}) = (e_{xx}-e_{yy})/2$; and $e_1(\Gamma_{5g}) = e_{xz}$, $e_2(\Gamma_{5g}) = e_{yz}$, and $e_3(\Gamma_{5g}) = e_{xy}$. We consider here the electron–deformation interaction linear in lattice strains:

$$H_{\rm ed} = \sum_{pk}\sum_{\alpha\beta} B^k_{p,\alpha\beta} e_{\alpha\beta} O^k_p = V(\Gamma_{1g})e(\Gamma_{1g}) + \sum_{\lambda=1,2} V_\lambda(\Gamma_{3g})e_\lambda(\Gamma_{3g}) + \sum_{\lambda=1:3} V_\lambda(\Gamma_{5g})e_\lambda(\Gamma_{5g}). \tag{3}$$

Parameters $B^k_{p,\alpha\beta}$ determine variations of the crystal field in the uniformly deformed crystal lattice [Eq. (23)]. The totally symmetric deformation is not taken into account, because it does not contribute to the splitting of a degenerate electronic state. Explicit forms of the electronic operators $V_\lambda(\Gamma)$ defined by seven independent parameters $b_p(\Gamma)$ are as follows:[20]

$$V_1(\Gamma_3) = b_2(\Gamma_3)O_2^0 + b_4(\Gamma_3)\big(O_4^0 - 7O_4^4\big) + b_6(\Gamma_3)\big(O_6^0 + 3O_6^4\big), \tag{4}$$

$$V_2(\Gamma_3) = \sqrt{3}\big[b_2(\Gamma_3)O_2^2 - 4b_4(\Gamma_3)O_4^2 + \tfrac{1}{2}b_6(\Gamma_3)\big(5O_6^2 + 11O_6^6\big)\big], \tag{5}$$

$$V_1(\Gamma_5) = 2b_2(\Gamma_5)O_2^1 - \tfrac{1}{2}b_4(\Gamma_5)\big(O_4^1 + 7O_4^3\big) + \tfrac{1}{4}b_6(\Gamma_5)\big(O_6^1 + \tfrac{9}{2}O_6^3 + \tfrac{33}{2}O_6^5\big) + \tfrac{3}{4}b'_6(\Gamma_5)\big(O_6^1 - \tfrac{5}{6}O_6^3 + \tfrac{1}{2}O_6^5\big), \tag{6}$$

$$V_2(\Gamma_5) = 2b_2(\Gamma_5)O_2^{-1} - \tfrac{1}{2}b_4(\Gamma_5)\big(O_4^{-1} - 7O_4^{-3}\big) + \tfrac{1}{4}b_6(\Gamma_5)\big(O_6^{-1} - \tfrac{9}{2}O_6^{-3} + \tfrac{33}{2}O_6^{-5}\big) + \tfrac{3}{4}b'_6(\Gamma_5)\big(O_6^{-1} + \tfrac{5}{6}O_6^{-3} + \tfrac{1}{2}O_6^{-5}\big), \tag{7}$$

$$V_3(\Gamma_5) = b_2(\Gamma_5)O_2^{-2} + b_4(\Gamma_5)O_4^{-2} + b_6(\Gamma_5)O_6^{-2} + b'_6(\Gamma_5)O_6^{-6}. \tag{8}$$

Values of the parameters $b_p(\Gamma)$ are calculated in Sec. III D.

Let E_n and $|n\xi\rangle$ ($\xi = 1 \div g_n$) be the eigenvalues and the corresponding eigenfunctions of the Hamiltonian $H_0 + H_{\rm CF}$. The envelope of the absorption (emission) spectrum in the region of the zero-phonon transition $n \to n'$ is given by the expression

$$I(\omega_{n'n} + \omega) \sim (2\pi\Delta^2)^{-1/2} \int d\boldsymbol{e}\, g(\boldsymbol{e}) \sum_{\delta=1}^{g_n}\sum_{\delta'=1}^{g_{n'}} I^{\delta\delta'}_{nn'}(\boldsymbol{e}) \times \exp\{-[\hbar\omega - \varepsilon_{n'\delta'}(\boldsymbol{e}) + \varepsilon_{n\delta}(\boldsymbol{e})]^2/2\Delta^2\}. \tag{9}$$

Here, $\omega_{n'n} = (E_{n'} - E_n)/\hbar$ is the frequency offset, $g(\boldsymbol{e})$ is the distribution function of random strains, and the Gaussian form function, with a half-width $(2\ln 2)^{1/2}\Delta$ considered as a fitting parameter, is introduced to account for a broadening of individual transitions (the values of Δ used in calculations described later are given in Table I). This broadening comes, in particular, from magnetic dipole–dipole interactions between impurity ions, superhyperfine interactions between the impurity ions and the fluorine nuclei, and random variations of the totally symmetric crystal field. Frequencies of transitions between sublevels of the initial (n) and final (n') energy levels are determined by eigenvalues $\varepsilon_{n\delta}$ of the perturbation $H_{\rm ed}$ in the basis of $|n\xi\rangle$ functions (the corresponding eigenfunctions being $|n\tilde{\delta}\rangle$), while the relative intensities of these transitions induced by the nonpolarized radiation equal

$$I^{\delta\delta'}_{nn'} = \sum_{\alpha=x,y,z} |\langle n'\tilde{\delta}'|m_\alpha|n\tilde{\delta}\rangle|^2, \tag{10}$$

where $\boldsymbol{m}$ is the magnetic moment operator of the R ion (zero-phonon electric dipole intraconfiguration transitions in R ions at sites with O_h symmetry are forbidden by parity considerations). Thus, to simulate the spectral envelope, the distribution function for random lattice strains is needed, and energy levels and relative transition probabilities as functions of the deformation tensor components have to be calculated. In the present work, it is assumed that the strains are induced

by point dilatation (compression) defects, and an explicit expression for the generalized distribution function of local strains is derived in Sec. III C. In Sec. III B, a possible influence of hyperfine interactions on the observed line profiles is analyzed.

B. Hyperfine structure of optical transitions in the odd isotopes of the R^{3+} ions (R = Yb, Er, Sm)

In the case of odd R isotopes with a nonzero nuclear spin moment I, the Hamiltonian in Eq. (1) contains additional terms corresponding to hyperfine interactions. Usually, the most important is the magnetic hyperfine interaction

$$H_{\mathrm{HF}} = \mu_B \gamma_N \hbar \left\langle \frac{1}{r^3} \right\rangle_{4f} \sum \{ 2\boldsymbol{I}\boldsymbol{l} + O_2^0(3 s_z I_z - \boldsymbol{s}\boldsymbol{I}) + 3O_2^2(s_x I_x - s_y I_y) + 3O_2^{-2}(s_x I_y + s_y I_x) + 6O_2^1(s_x I_z + s_z I_x) + 6O_2^{-1}(s_z I_y + s_y I_z) \}, \quad (11)$$

which results in a line splitting that can be observed in high-resolution spectra (e.g., Ref. 21, where the resolved hyperfine structure in the spectra of $LiYF_4$:$^{167}Er^{3+}$ was observed and successfully modeled). In Eq. (11), μ_B is the Bohr magneton; γ_N is the nuclear gyromagnetic ratio; the sum is taken over $4f$ electrons with radius vectors $\boldsymbol{r}$, orbital moments $\boldsymbol{l}$, and spin moments $\boldsymbol{s}$; and $\langle 1/r^3 \rangle_{4f}$ is the expectation value of the $1/r^3$ operator over a $4f$-electron wave function. In this case, the spectral envelopes can be simulated considering the energies $\varepsilon_{n\delta}$ in Eq. (9) and the ket vectors $|n\tilde{\delta}\rangle$ in Eq. (10) as eigenvalues and eigenfunctions of the perturbation $H_{\mathrm{HF}} + H_{\mathrm{ed}}$ operating in the space of $(2I+1)g_n$ electron-nuclear states $|n\xi\rangle|I, I_z\rangle$.

There are several even isotopes and two odd isotopes of ytterbium, i.e., ^{171}Yb and ^{173}Yb ($I = 1/2$ and $I = 5/2$, respectively; Table II). Energies of electron-nuclear states of the odd ytterbium isotopes were obtained from numerical diagonalization of the Hamiltonian $H_0 + H_{\mathrm{CF}} + H_{\mathrm{HF}}$ in the space of states of the $4f^{13}$ configuration with dimensions of 28 and 84 for the $^{171}Yb^{3+}$ and $^{173}Yb^{3+}$ ions, respectively. For this configuration, H_0 involves only the spin–orbit interaction with the coupling constant $\zeta = 2913$ cm^{-1};[11] the crystal-field parameters are given in Table I. The electron-nuclear states can be characterized by the total angular momentum $\boldsymbol{F} = \boldsymbol{S} + \boldsymbol{I}$, where the effective spin S equals 1/2 or 3/2 for crystal-field states of the Γ_6, Γ_7 or the Γ_8 symmetry, respectively.

TABLE II. Parameters for odd R isotopes used in simulations of the hyperfine structure.[a]

	^{147}Sm	^{149}Sm	^{167}Er	^{169}Tm	^{171}Yb	^{173}Yb
Natural abundance (%)	15	13.8	22.9	100	14.3	16.2
Nuclear spin I	7/2	7/2	7/2	1/2	1/2	5/2
Gyromagnetic ratio $\gamma_N/2\pi$ (MHz/T)	−1.775	−1.46	−1.23	−3.53	7.53	−2.07
$\langle 1/r^3 \rangle_{4f}$ (at. units)	6.5	6.5	11.07	11.73	12.5	12.5

[a]References 22 and 23.

The ground state $\Gamma_6(^2F_{7/2}) \times D^{(1/2)}$ ($D^{(l)}$ is the irreducible representation of the rotation group) of the $^{171}Yb^{3+}$ ion is split by the hyperfine interaction [Eq. (11)] into a singlet Γ_1 ($F = 0$) and a triplet Γ_4 ($F = 1$) with a gap of 0.069 cm^{-1}. The excited crystal-field level $\Gamma_8(^2F_{5/2}) \times D^{(1/2)}$ splits into three electron-nuclear sublevels $\Gamma_3 + \Gamma_4 + \Gamma_5$, the total splitting being 0.16 cm^{-1}. Four magnetic dipole transitions are allowed within the spectral line $^2F_{7/2}(\Gamma_6) \rightarrow {}^2F_{5/2}(\Gamma_8)$, i.e., $\Gamma_1 \rightarrow \Gamma_4$, $\Gamma_4 \rightarrow \Gamma_3, \Gamma_4, \Gamma_5$; their wave numbers differ by no more than 0.16 cm^{-1}.

In the spectrum of the $^{173}Yb^{3+}$ ions, the ground state $\Gamma_6(^2F_{7/2}) \times D^{(5/2)}$ splits into two sets of quasidegenerate electron-nuclear sublevels, $\Gamma_2 + \Gamma_4 + \Gamma_5$ ($F = 3$) and $\Gamma_3 + \Gamma_5$ ($F = 2$), with a gap of 0.057 cm^{-1}, and the excited state $\Gamma_8(^2F_{5/2}) \times D^{(5/2)}$ splits into 10 sublevels, $\Gamma_1 + \Gamma_2 + 2\Gamma_3 + 3\Gamma_4 + 3\Gamma_5$, corresponding to $F = 1, 2, 3, 4$, with a total splitting of 0.159 cm^{-1}. The inset in Fig. 1 displays the sum of spectral envelopes for even and odd isotopes calculated according to Eq. (9) using parameters from Table II and neglecting random lattice strains. Due to a number of allowed magnetic dipole transitions between the electron-nuclear sublevels, integral intensities of individual transitions in the odd ytterbium isotopes are considerably lower than the intensity of a single transition in the even isotopes. The total width of the hyperfine structure of the $^2F_{7/2}(\Gamma_6) \rightarrow {}^2F_{5/2}(\Gamma_8)$ transition is about two times smaller than the width of the dip in the observed spectral line of the sample with the lowest nominal concentration (0.01 at.%) of Yb^{3+} ions. In real crystals, because of additional broadening and splitting of spectral lines due to random lattice strains, the contribution of the odd isotopes into the observed spectrum is presented by a smooth background under the central line.

There is only one stable odd erbium isotope: ^{167}Er, with the nuclear spin $I = 7/2$. Figure 3(a) (curve 1) shows the sum of spectral envelopes in the region of the $^4I_{15/2}(\Gamma_8) \rightarrow {}^4I_{13/2}(\Gamma_6)$ transition in even and odd isotopes of Er^{3+}, calculated for the perfect cubic lattice using Eq. (9). Energies and wave functions of the crystal-field states for even isotopes were obtained from diagonalization of the electronic Hamiltonian $H_0 + H_{\mathrm{CF}}$ in the space of 364 states of the $4f^{11}$ configuration. Parameters of the free-ion Hamiltonian were taken from Ref. 13; the crystal-field parameters are given in Table I. Furthermore, the energies and wave functions of electron-nuclear states for the odd isotope were obtained from diagonalization of the Hamiltonian H_{HF} projected onto the truncated space of 240 electron-nuclear states corresponding to crystal-field sublevels of the $^4I_{13/2}$ and $^4I_{15/2}$ multiplets. The ground state $\Gamma_8(^4I_{15/2}) \times D^{(7/2)}$ of the $^{167}Er^{3+}$ ion splits into four sets of sublevels ($F = 5$, 4, 3, and 2), $\Gamma_3 + 2\Gamma_4 + \Gamma_5$, $\Gamma_1 + \Gamma_3 + \Gamma_4 + \Gamma_5$, $\Gamma_2 + \Gamma_4 + \Gamma_5$, and $\Gamma_3 + \Gamma_5$, whereas the total splitting equals 0.176 cm^{-1}. The excited state $\Gamma_7(^4I_{13/2}) \times D^{(7/2)}$ splits into two groups of quasidegenerate states, $\Gamma_1 + \Gamma_3 + \Gamma_4 + \Gamma_5$ ($F = 4$) and $\Gamma_2 + \Gamma_4 + \Gamma_5$ ($F = 3$), with a gap of 0.099 cm^{-1}. The calculated width of the hyperfine structure of the transition $^4I_{15/2}(\Gamma_8) \rightarrow {}^4I_{13/2}(\Gamma_6)$ considerably exceeds the width of the dip in the measured spectral envelope; this structure may be responsible for the weak shoulders close to the center of the observed line [Fig. 3(a)].

Samarium also has several even isotopes and two odd isotopes, ^{147}Sm and ^{149}Sm (Table II), with nuclear spin $I = 7/2$ for each. Calculated hyperfine splitting of the ground $\Gamma_7(^6H_{5/2})\times D^{(7/2)}$ and the excited $\Gamma_8(^6H_{13/2})\times D^{(7/2)}$ states is more than four times smaller than the width of the dip in the observed spectral line for the $^6H_{5/2}(\Gamma_7) \rightarrow {}^6H_{13/2}(\Gamma_8)$ transition in the spectrum of the sample Cs_2NaYF_6:Sm^{3+} (3 at.%). Thus, the results of calculations give evidence that the observed fine structures are not related to hyperfine splitting in the spectra of the odd isotopes of the trivalent Yb, Er, and Sm ions.

C. Generalized distribution function of local strains produced by random point defects in the elastic continuum

Let us consider the strain field $e_{\alpha\beta}(\boldsymbol{r})$ produced by N_d point defects placed at the points $\boldsymbol{R}_j(x_j,y_j,z_j)$ $(j = 1\ldots N_d)$ in the elastic continuum. In the Cartesian coordinate frame, strains due to a single defect are determined by the expression[24,25]

$$e^j_{\alpha\beta} = \frac{A}{r_j^3}\left(\delta_{\alpha\beta} - 3\frac{x_{j\alpha}x_{j\beta}}{r_j^2}\right). \tag{12}$$

Here, $x_{j\alpha}$ are components of the vector $\boldsymbol{r}_j = \boldsymbol{r} - \boldsymbol{R}_j$ and $A = (\Omega/12\pi)(1+\sigma)/(1-\sigma)$ is the defect strength that depends on the Poisson coefficient of a crystal σ and the change $\Omega = dV/dN_d$ of a sample volume V due to a single defect.[16,25] Because, according to Eq. (12), $e^j_{xx} + e^j_{yy} + e^j_{zz} = 0$, we may consider five independent normalized combinations of the deformation tensor components (12), with the angular parts corresponding to tesseral harmonics of the second order:

$$\begin{aligned}
e^j_1 &= e^j_1(\Gamma_{3g}) = -\frac{\sqrt{3}A}{2r_j^5}\left(2z_j^2 - x_j^2 - y_j^2\right),\\
e^j_2 &= e^j_2(\Gamma_{3g}) = -\frac{3A}{2r_j^5}\left(x_j^2 - y_j^2\right), \quad e^j_3 = e^j_1(\Gamma_{5g}) = -\frac{3Ax_jz_j}{r_j^5},\\
e^j_4 &= e^j_2(\Gamma_{5g}) = -\frac{3Ay_jz_j}{r_j^5}, \quad e^j_5 = e^j_3(\Gamma_{5g}) = -\frac{3Ax_jy_j}{r_j^5}.
\end{aligned} \tag{13}$$

In the case of a low concentration of defects, it is natural to assume that strains due to different defects are additive. Then, the distribution function $g(e_1,e_2,e_3,e_4,e_5) \equiv g(\boldsymbol{e})$ can be presented as follows:

$$g(\boldsymbol{e}) = \left\langle \prod_{m=1}^{5} \delta\left(e_m - \sum_j e^j_m\right)\right\rangle, \tag{14}$$

where $\delta(\ldots)$ is the Dirac delta function and $\langle\ldots\rangle$ denotes the averaging over random coordinates of N_d identical point defects. Under the assumption that defects occupy random positions within the crystal, the averaging is replaced by N_d integrals over the crystal volume. The substitution of delta function with its integral representation and the application of the limit $N_d, V \rightarrow \infty$ under the condition of the fixed defect concentration $N_d/V = C_d$ give the following expression:

$$\begin{aligned}
g(\boldsymbol{e}) &= \frac{1}{(2\pi)^5 V^{N_d}} \int_{-\infty}^{\infty} d\rho_1 \ldots \int_{-\infty}^{\infty} d\rho_5 \\
&\times \int_V dV_1 \int_V dV_2 \ldots \int_V dV_{N_d} \\
&\times \exp\left[i \sum_{m=1}^{5} \rho_m \left(\sum_j e^j_m - e_m \right) \right] \\
&= \frac{1}{(2\pi)^5} \int_{-\infty}^{\infty} d\rho_1 \ldots \int_{-\infty}^{\infty} d\rho_5 \\
&\times \exp\left[-i \sum_{m=1}^{5} \rho_m e_m - C_d J(\rho_1,\ldots,\rho_5) \right],
\end{aligned} \tag{15}$$

where

$$J(\rho_1,\ldots,\rho_5) = \int_V d^3\boldsymbol{r} \left[1 - \exp\left(i \sum_{m=1}^{5} \rho_m e_m(\boldsymbol{r}) \right) \right]. \tag{16}$$

Let us introduce the coordinates $\tilde{x},\tilde{y},\tilde{z}$ connected with x,y,z by the orthogonal transformation that brings about the diagonal quadratic form

$$r^5 \sum_{m=1}^{5} \rho_m e_m(\mathbf{r}) = \sum_{\alpha,\beta=x,y,z} c_{\alpha\beta}x_\alpha x_\beta = \tilde{c}_x\tilde{x}^2 + \tilde{c}_y\tilde{y}^2 + \tilde{c}_z\tilde{z}^2. \tag{17}$$

Using the definitions (13), we can rewrite Eq. (17) as $\sum_{m=1}^{5} \rho_m e_m(\boldsymbol{r}) = \tilde{\rho}_1\tilde{e}_1(\boldsymbol{r}) + \tilde{\rho}_2\tilde{e}_2(\boldsymbol{r})$, where the coefficients $\tilde{\rho}_1$ and $\tilde{\rho}_2$ are connected with ρ_m by the equation $\tilde{\rho}_1^2 + \tilde{\rho}_2^2 = \sum_{m=1}^{5} \rho_m^2 \equiv \rho^2$. Now, the integral in Eq. (16) can be obtained in the analytical form by using the spherical coordinates r,θ,φ of the vector $\boldsymbol{r}(\tilde{x},\tilde{y},\tilde{z})$:

$$J(\rho_1,\ldots,\rho_5) = \frac{4\pi^2|A|\rho}{9}[\beta(\eta) - i\beta'(\eta)\mathrm{sgn}(A)]. \tag{18}$$

Here, $\eta = \arctan(\tilde{\rho}_2/\tilde{\rho}_1)$ and

$$\begin{aligned}
\beta(\eta) &= \frac{3}{8\pi}\int \sin\theta d\theta d\varphi |\psi|,\\
\beta'(\eta) &= \frac{3}{4\pi^2}\int \sin\theta d\theta d\varphi \psi \ln|\psi|,
\end{aligned} \tag{19}$$

where $\psi(\theta,\varphi) = r^3(\tilde{\rho}_1\tilde{e}_1 + \tilde{\rho}_2\tilde{e}_2)/A\rho$. As shown in Ref. 26, the function $\beta(\eta)$ slightly differs from unity in the whole interval of η values $[(3/\pi) \leqslant \beta(\eta) \leqslant 1]$, and the function $\beta'(\eta)$ with alternating signs satisfies the inequality $|\beta'(\eta)| \leqslant \beta'(0) = \frac{3\sqrt{3}}{2\pi}\int_0^1 dx(3x^2-1)\ln|3x^2-1| < 0.132$. Because of these inequalities, approximate constant values of the functions $\beta(\eta) = 1$ and $\beta'(\eta) = 0$ can be used. Now it is easy to obtain the analytical form of the distribution in Eq. (15). The sum $\sum_{m=1}^{5} \rho_m e_m$ can be considered the scalar product of the five-dimensional vectors $\boldsymbol{\rho}$ and $\boldsymbol{e}$. The integral over variables ρ_m is calculated using hyperspherical coordinates $(\rho,\theta_1,\theta_2,\theta_3,\theta_4)$ and the equality $(\boldsymbol{\rho}\cdot\boldsymbol{e}) = \rho e\cos\theta_1$, where

$e^2 = \sum_{m=1}^{5} e_m^2$:

$$g(\boldsymbol{e}) = \frac{1}{(2\pi)^5}\int_0^\infty \rho^4 d\rho \exp\left(-\frac{4\pi^2 C_d\,|A|\,\rho}{9}\right)\int_0^\pi \sin^3\theta_1 d\theta_1 \times \exp(-i\rho e\cos\theta_1)\int_0^\pi \sin^2\theta_2 d\theta_2 \int_0^\pi \sin\theta_3 d\theta_3 \int_0^{2\pi} d\theta_4$$
$$= \frac{1}{4\pi^3 e^3}\int_0^\infty \rho d\rho \exp\left(-\frac{4\pi^2 C_d |A|\rho}{9}\right) \times [\sin(\rho e) - \rho e\cos(\rho e)]$$
$$= \frac{2\gamma}{\pi^3(e^2+\gamma^2)^3}. \quad (20)$$

The width of the distribution, $\gamma = \frac{\pi(1+\sigma)}{27(1-\sigma)}\frac{d\ln v}{d\ln C_d}$, is determined by the Poisson coefficient σ and the unit cell volume v dependence on the concentration C_d of point lattice defects.

The subsequent integrations of $g(\boldsymbol{e})$ over e_m results in the well-known one- and two-dimensional distributions:[16,26]

$$g(e_1) = \frac{\gamma}{\pi\left(e_1^2+\gamma^2\right)}, \quad g(e_1,e_2) = \frac{\gamma}{2\pi\left(e_1^2+e_2^2+\gamma^2\right)^{3/2}}. \quad (21)$$

D. Electron–deformation coupling constants

Parameters $b_p(\Gamma)$ of the electron–deformation interaction were calculated within the framework of the exchange charge model.[20,27,28] In line with this model, parameters of the crystal field affecting the impurity R ions are presented as the sums of contributions due to the electrostatic fields of effective point charges of the host lattice ions: $B_p^k = \sum_L B_p^k(\boldsymbol{R}_L)$ (here, the lattice ions are labeled L and have the spherical coordinates R_L, θ_L,φ_L relative to the R ion placed at the origin of the system of coordinates). However, in contrast to the simple point–charge model, the effective charges $q_L^{(p)}$ of the nearest-neighbor lattice ions (ligands) involve exchange charges, which depend on the rank p of the $4f$ electron multipolar moment and are related to the overlap integrals between the electronic $4f$ and the ligand wave functions:[27]

$$q_L^{(p)} = q_L - \frac{2(2p+1)R_L^p}{7(1-\sigma_p)\langle r^p\rangle_{4f}} S_p(R_L). \quad (22)$$

Here, eq_L is the nominal charge of an ion (e is the proton charge), σ_p are the shielding constants,[29] and $S_p(R_L) = G_\sigma S_\sigma(R_L)^2 + \gamma_p G_\pi S_\pi(R_L)^2$ are the quadratic forms constructed from the overlap integrals $S_\sigma(R_L) = \langle 4\,3\,0(R)|2\,1\,0(L)\rangle$ and $S_\pi(R_L) = \langle 4\,3\,1(R)|2\,1\,1(L)\rangle$, where one-electron wave functions of the R and the ligand (fluorine) ions $|n\,l\,l_z\rangle$ are defined by the principle quantum number n, orbital moment l, and its projection l_z and are considered in the reference frame with the common quantization axis along the vector $\boldsymbol{R}_L$. Also, $\gamma_p = 2 - p(p+1)/12$, and G_σ, G_π are dimensionless parameters of the model. The moments of the $4f$-electron density $\langle r^p\rangle_{4f}$ ($p = 2, 4, 6$) and overlap integrals were calculated using radial wave functions of the R and fluorine ions given in Refs. 30 and 31. Furthermore, we determined the values of the model parameters G_σ = 21, 22.1, 20.5, 11.2 and G_π = 45, 23, 19.5, 8 for Yb^{3+}, Tm^{3+}, Er^{3+}, and Sm^{3+}, respectively, from a comparison of the calculated and experimental values of the parameters B_4 and B_6 (Table I). Thus, we obtained the crystal-field parameters and parameters of the electron–deformation interaction $B_{p,\alpha\beta}^k$ in the Hamiltonian given by Eq. (3),

$$B_{p,\alpha\beta}^k = \frac{1}{2}\sum_L \left(X_{L\beta}\frac{\partial}{\partial X_{L\alpha}} + X_{L\alpha}\frac{\partial}{\partial X_{L\beta}}\right) B_p^k(\boldsymbol{R}_L), \quad (23)$$

as explicit functions of the coordinates of the lattice ions. According to Eqs. (4)–(8), the parameters $b_p(\Gamma)$ and $B_{p,\alpha\beta}^k$ are connected by the following relations [Eq. (3)]:

$$b_p(\Gamma_3) = 2\left(B_{p,zz}^0 - B_{p,xx}^0\right)/\sqrt{3}, \quad b_p(\Gamma_5) = 2B_{p,xy}^{-2}, \quad b_6'(\Gamma_5) = 2B_{6,xy}^{-6}. \quad (24)$$

The calculated values of the parameters $b_p(\Gamma)$ are given in Table III. In the present work, to avoid introduction of additional unknown parameters that determine the coupling between macro- and microdeformations, we neglected renormalization of the parameters $b_p(\Gamma)$ due to the interaction of the R ions with the sublattice displacements of the Γ_{3g} and Γ_{5g} symmetry.

TABLE III. Parameters of the electron–deformation interaction (in cm^{-1}) for Cs_2NaYF_6:R^{3+} (R = Yb, Tm, Er, Sm).

	Yb	Tm	Er	Sm
$b_2(\Gamma_3)$	−12850	−11570	−11550	−11100
$b_4(\Gamma_3)$	−1018	−1078	−1100	−1127
$b_6(\Gamma_3)$	350	−422	−470	−444
$b_2(\Gamma_5)$	7760	7482	7488	7638
$b_4(\Gamma_5)$	−1544	−1685	−1768	−2094
$b_6(\Gamma_5)$	−70	573	646	782
$b_6'(\Gamma_5)$	−440	3800	4282	5190

E. Simulations of spectral profiles and comparison with the measured spectra

In the space of four states belonging to the Γ_8 quadruplet, the Hamiltonian H_{ed} of the R ion interacting with strains of the $\Gamma_{3g}(e_1, e_2)$ and $\Gamma_{5g}(e_3, e_4, e_5)$ symmetry is determined by two real parameters $v(\Gamma_{3g})$ and $v(\Gamma_{5g})$, which equal to corresponding matrix elements of the operators in Eqs. (4)–(8) and can be represented by 2×2 blocks as follows:

$$\langle\Gamma_8|H_{ed}|\Gamma_8\rangle = \begin{vmatrix} v(\Gamma_{3g})(-\sigma_z e_1 + \sigma_x e_2) + v(\Gamma_{5g})\sigma_y e_5 & v(\Gamma_{5g})\sigma_z(e_3 - ie_4) \\ v(\Gamma_{5g})\sigma_z(e_3 + ie_4) & v(\Gamma_{3g})(\sigma_z e_1 - \sigma_x e_2) - v(\Gamma_{5g})\sigma_y e_5 \end{vmatrix}, \quad (25)$$

where σ_α are the Pauli matrices. Calculated values of $v(\Gamma_{3g})$ and $v(\Gamma_{5g})$ for quadruplets involved in the transitions with the observed fine structure are given in Table I. It is seen from Table I that the Yb^{3+} ions with the largest electron–deformation coupling constants are the most sensitive probes of lattice strains.

The matrix in Eq. (25) is easily diagonalized, and it has two degenerate eigenvalues. Thus, in the deformed lattice, the quadruplet splits into two doublets with energies $\pm E$ depending on the two independent variables $\rho = (e_1^2 + e_2^2)^{1/2}$ and $r = (e_3^2 + e_4^2 + e_5^2)^{1/2}$ only:

$$E = [v(\Gamma_{3g})^2\rho^2 + v(\Gamma_{5g})^2 r^2]^{1/2}. \quad (26)$$

Now we can substitute the distribution function (20) for $g(\boldsymbol{e})$ and energies $\pm E$ for $\varepsilon_{n\delta}$ into Eq. (9). Because the integral intensities of magnetic dipole transitions induced by the nonpolarized radiation between the Γ_6 or Γ_7 doublets and the different Γ_8 sublevels are the same, we obtain the following spectral envelope of the doublet–quadruplet transitions:

$$I(\omega_{n'n} + \omega) \sim \int_0^\infty \rho d\rho \int_0^\infty r^2 dr \times \left[\left(\frac{\rho}{v(\Gamma_{3g})}\right)^2 + \left(\frac{r}{v(\Gamma_{5g})}\right)^2 + 1\right]^{-3} \times (\exp\{-[\hbar\omega - \gamma(\rho^2 + r^2)^{1/2}]^2/2\Delta^2\} + \exp\{-[\hbar\omega + \gamma(\rho^2 + r^2)^{1/2}]^2/2\Delta^2\}). \quad (27)$$

The computed spectral envelopes for doublet–quadruplet transitions in the even isotopes of the Yb^{3+}, Er^{3+}, and Sm^{3+} ions are compared with the measured line shapes in Figs. 1–3. The width γ of the distribution function $g(\boldsymbol{e})$ was varied to fit the measured spectral positions of the two maxima of the split absorption line. As seen from Figs. 1–3, the dips in the spectral profiles near line centers are well reproduced by calculations. The obtained values of the most probable strains of the Γ_{3g} ($\rho_M = \gamma/\sqrt{3}$) and Γ_{5g} ($r_M = \gamma\sqrt{2/3}$) symmetry and their variations with the type of the host ions and the concentration of the impurity ions (Table I) are physically reasonable. Low values of γ (3×10^{-5}–4×10^{-5}) in yttrium elpasolites weakly doped with Er^{3+} or Yb^{3+} ions can be associated mainly with intrinsic lattice defects. Because the differences among the ionic radii R of Er^{3+} ($R_{Er} = 0.089$ nm, here and later the ionic radii corresponding to the sixfold coordination are indicated[32]), Yb^{3+} ($R_{Yb} = 0.0868$ nm), and Y^{3+} ($R_Y = 0.09$ nm) are rather small, perturbations of the lattice by the impurity ions in these crystals can be neglected. Alternatively, the Sm^{3+} ion has a considerably larger ionic radius, $R_{Sm} = 0.0958$ nm, and induces local lattice expansion when substituting for the host Y^{3+} ion. Correspondingly, the width γ of the strain distribution function and the width Δ of the individual transitions in the Sm^{3+}-doped yttrium elpasolite are about an order of magnitude larger than γ and Δ in the yttrium elpasolites containing comparable concentrations of the impurity Er^{3+} or Yb^{3+} ions (Table I). An even more pronounced effect caused by lattice deformations due to the impurity R ions was found in the scandium elpasolites doped with the Yb^{3+} ions, where the difference between the ionic radii of the host Sc^{3+} ($R_{Sc} = 0.0745$ nm) and the impurity ions ($R_{Yb} = 0.0868$ nm) is rather large. In these scandium crystals, the strain distribution width γ increases markedly with the concentration of the impurity Yb^{3+} ions; in particular, γ changes sixfold in Cs_2NaScF_6 crystals when the nominal ytterbium concentration c increases 20 times (Table I). Supposing that concentrations of intrinsic defects are the same in the samples of Cs_2NaScF_6 with different concentrations of ytterbium, we find that the contributions into the widths γ due to the impurity Yb^{3+} ions equal 1.25×10^{-5} and 24.9×10^{-5} for $c = 0.1$ and 2 at.%, respectively.

Finally, let us consider the line shape of the transition $\Gamma_1(^3H_6) \rightarrow \Gamma_4(^3H_5)$ in the Tm^{3+} ions. There is only one stable thulium isotope, ^{169}Tm, with nuclear spin $I = 1/2$ (Table II). The energies and wave functions of the Tm^{3+} ion in the perfect lattice of Cs_2NaYF_6 were obtained from diagonalization of the Hamiltonian $H_0 + H_{CF} + H_{HF}$ in the total space of 182 electron-nuclear states of the electronic $4f^{12}$ configuration. Parameters of the free-ion Hamiltonian and crystal-field parameters were taken from Ref. 13. The ground state transforms according to the $\Gamma_1(^3H_6) \times D^{(1/2)} = \Gamma_6$ irreducible representation of the double O_h group, and the lowest crystal-field sublevel Γ_4 of the $^3H_5$ multiplet is split by the hyperfine interaction into a Γ_6 doublet and a Γ_8 quadruplet, with a gap of $E_0 = 0.062$ cm^{-1}. The calculated line shape of the transition $\Gamma_1(^3H_6) \rightarrow \Gamma_4(^3H_5)$ in the perfect lattice is shown in Fig. 4 (curve 1). It differs remarkably from the observed line shape, which shows a splitting of the high-frequency component comparable to the gap induced by the hyperfine interaction. Thus, because the hyperfine splitting and the strain-induced splitting have comparable values, we must consider the sum of the hyperfine and the electron–deformation interactions to be a perturbation. The projection h of the Hamiltonian $H_{HF} + H_{ed}$ on the space of six electron-nuclear states $\Gamma_4 \times D^{(1/2)} = \Gamma_6 + \Gamma_8$ can be presented as follows:

$$h = \begin{vmatrix} -E_0 \cdot \hat{1} & h_{12} & h_{13} \\ h_{12}^+ & h_{22} & h_{23} \\ h_{13}^+ & h_{23}^+ & -h_{22} \end{vmatrix}, \quad (28)$$

where $\hat{1}$ is the unit 2×2 matrix, $h_{12} = -\sqrt{2}iv(\Gamma_{3g})e_2\sigma_y - v(\Gamma_{5g})(e_3 \cdot \hat{1} + ie_4\sigma_z - 2ie_5\sigma_x)$, $h_{13} = \sqrt{2}v(\Gamma_{3g})e_1\sigma_z - \sqrt{3}v(\Gamma_{5g})(e_3\sigma_x + e_4\sigma_y)$, $h_{22} = v(\Gamma_{3g})e_1 \cdot \hat{1}$, and $h_{23} = -v(\Gamma_{3g})e_2\sigma_x + \sqrt{2}v(\Gamma_{5g})(e_3\sigma_z - ie_4 \cdot \hat{1} - ie_5\sigma_y)$. The calculated values of $v(\Gamma_{3g})$ and $v(\Gamma_{5g})$ are given in Table I. The computation of the spectral envelope according to Eq. (9) involved numerical diagonalization of the matrix in Eq. (28) and calculations of the relative integral intensities in Eq. (10) for each set of the strain tensor components. The obtained envelopes (Fig. 4, curves 2A and 2B) contain a central peak and two wings with approximately equal intensities. Such distribution of the line intensity agrees with the observed shape of the $\Gamma_1(3H_6) \rightarrow \Gamma_4(^3H_5)$ transition in the Cs_2NaYF_6 sample containing 1 at.% of Tm^{3+}; however, it differs markedly from the measured line shapes in the spectra of the weakly doped samples where the high-frequency wing is more intense than the low-frequency one. It is possible that this asymmetry of the wings is not reproduced by calculations, because elastic anisotropy of the crystal lattice has been neglected when deriving the strain distribution function. Also, weak residual quasiuniform strains may contribute to a redistribution of the

wing intensities. The obtained widths of the strain distribution function in the Cs_2NaYF_6 samples containing 0.1 and 1.0 at.% of Tm^{3+}, $\gamma = 6 \times 10^{-5}$ and 15×10^{-5}, respectively, correlate with the values of γ in the samples doped with comparable concentrations of Yb^{3+} (Table I) and the value of 8.5×10^{-5} obtained earlier for the $LiYF_4$:Ho^{3+} (0.1 at.%) crystal containing Tm^{3+} as a trace impurity.[4]

In conclusion, we turn to the satellites of the spectral lines corresponding to the doublet–quadruplet transitions, which are observed in the Cs_2NaYF_6 and Cs_2NaScF_6 samples containing enhanced concentrations of Yb^{3+} or Er^{3+} [Figs. 1(b), 2(b), and 3(a)]. We could suppose that the quadruplets in the pair centers formed by the nearest-neighbor R ions, e.g., ions R_1 and R_2, are split due to local lattice deformations and magnetic dipole and exchange interactions. However, in the elpasolite structure, the impurity R ions have no common ligands, i.e., fluorine ions, and the minimum distance $a/\sqrt{2} \approx 0.65$ nm (a is the lattice constant) between the R_1 and the R_2 ions is so large that the energy of magnetic interactions in, e.g., Yb^{3+}-doped crystals is negligible compared to the observed shifts $\hbar\Delta\omega$ of the satellites from the central line. In the case of the Cs_2NaScF_6:Yb^{3+} crystals, a crude estimation of contributions into the crystal field affecting the Yb_1 ion due to electrostatic fields of six fluorine ions in the first coordination shell of the Yb_2 ion, shifted by $R_{Yb} - R_{Sc} = 0.012$ nm to new equilibrium positions, results in the splitting of the $\Gamma_8(^2F_{5/2})$ level equal to 0.68 cm^{-1}, which is ~20 times less than the measured splitting $2\hbar\Delta\omega$. The detailed analysis of the lattice relaxation in the vicinity of an impurity dimer could give a bit larger splitting, but this task is beyond the scope of the present work. Because of a very strong interaction of the Yb^{3+} ions in the $\Gamma_8(^2F_{5/2})$ state with lattice strains, it is more likely that the satellites arise due to an effective coupling between the Yb^{3+} ions mediated by dynamic lattice deformations. Observation of low-temperature quadrupolar ordering in Cs_2NaHoF_6 evidences an important role of interactions between the R ions through the phonon field in fluoroelpasolites.[33] To reveal the basic physics of this interaction, we considered the following Hamiltonian of the ytterbium dimer:

$$H_d = H_0(R_1) + H_{CF}(R_1) + H_0(R_2) + H_{CF}(R_2) + H(R_1, R_2), \tag{29}$$

which operates in the space of $14 \times 14 = 196$ states belonging to the Kronecker product of single-ion states, where the two-body term was taken in the form

$$H(R_1, R_2) = -[V_1(\Gamma_{3g}, R_1)V_1(\Gamma_{3g}, R_2) + V_2(\Gamma_{3g}, R_1)V_2(\Gamma_{3g}, R_2)]/D \tag{30}$$

corresponding to the interion interaction through deformations of the Γ_{3g} symmetry induced by long-wave acoustic phonons only,[34] with the denominator D as a fitting parameter. By an order of magnitude, D should be comparable to $(C_{11} - C_{12})v \sim 10^6$ cm^{-1}, where C_{ij} are the elastic constants and v is the unit cell volume. The computed envelope of the magnetic dipole transitions from the lowest 4 states $[\Gamma_6(^2F_{7/2}, R_1) \times \Gamma_6(^2F_{7/2}, R_2)]$ to the 16 excited states $[\Gamma_8(^2F_{5/2}) \times \Gamma_6(^2F_{7/2}) + \Gamma_6(^2F_{7/2}) \times \Gamma_8(^2F_{5/2})]$ of a dimer with the Hamiltonian in Eq. (29) matches well the observed satellites in the Cs_2NaYF_6:Yb^{3+} (1 at.%) crystal, provided $D = 4.6 \times 10^6$ cm^{-1} and the width of individual transitions $\Delta = 0.15$ cm^{-1}, comparable to the width of the central line [Fig. 1(b), curve 2].

In the case of a pair of the nearest-neighbor Er^{3+} ions, the energy of the magnetic dipole–dipole interaction, which is comparable to the measured shifts of satellites from the central line, is added to the operator (30). The curve 3 in Fig. 3(a) represents the simulated spectral envelope of the transitions from the 16 lowest states $\Gamma_8(^4I_{15/2}, R_1) \times \Gamma_8(^4I_{15/2}, R_2)$ to the 16 excited states $\Gamma_8(^4I_{15/2}) \times \Gamma_6(^4I_{13/2}) + \Gamma_6(^4I_{13/2}) \times \Gamma_8(^4I_{15/2})$ of the erbium dimer containing even isotopes. Energies and wave functions were obtained from diagonalization of the two-body Hamiltonian in the space of $30 \times 30 = 900$ crystal-field states belonging to the $^4I_{15/2}$ and $^4I_{13/2}$ multiplets of Er^{3+}. We can see from Fig. 3(a) that the observed weak satellites in the spectrum of the Cs_2NaYF_6:Er^{3+} (0.3 at.%) crystal might be related to the fine structure of the computed envelope. However, our simulations show that the shape of the considered spectral envelope strongly depends on possible contributions of dynamic deformations with the Γ_{5g} symmetry into the interion interaction as well. Thus, to elucidate the main physical mechanisms responsible for formation of the satellites, more detailed spectroscopic studies of a concentration series for the R-doped fluoride crystals with the elpasolite structure are desirable.

IV. CONCLUSIONS

We have presented the first observation of the fine structures of spectral lines corresponding to optical intraconfiguration $4f$-$4f$ transitions in the R ions at sites with cubic O_h symmetry. The observed doublet structure of the doublet (Γ_6 or Γ_7)—quadruplet (Γ_8) transitions in the Kramers Yb^{3+}, Er^{3+}, and Sm^{3+} ions and the triplet structure of the singlet (Γ_1)—triplet (Γ_4) transitions in the non-Kramers Tm^{3+} ions were shown to be caused by splitting of the quadruplets or triplets in the random crystal fields of the tetragonal (Γ_{3g}) or trigonal (Γ_{5g}) symmetry. To treat the problem theoretically, an explicit expression for the generalized distribution function of local strains produced by random point defects in the elastic continuum was derived. The observed spectral profiles were reproduced by a model that involves only two fitting parameters: the width γ of the strain distribution and the line width Δ of individual single-ion transitions. The values of these parameters were found from the comparison of the simulated and measured line shapes. For all Cs_2NaYF_6 crystals weakly doped with different R ions, the obtained values of γ of the order of 10^{-5} are approximately the same, and correspondingly, random strains can be attributed to intrinsic lattice defects. However, a considerable increase of the width for the strain distribution with increasing concentration of impurity ions evidences the lattice perturbation due to a substitution of the R ion for the Y^{3+} ion. These local lattice perturbations are more pronounced in the R-doped Cs_2NaScF_6 crystals, which correlates with larger differences between the ionic radii of the impurity and the host ions. The observed satellite transitions were explained by considering the pairs of the nearest-neighbor R ions interacting through the dynamic lattice deformations.

ACKNOWLEDGMENTS

This work was supported by the Russian Foundation for Basic Research (Grant No. 12-02-31284), the Russian Academy of Sciences (under the program "Fundamental Optical Spectroscopy and Its Applications"), the Russian Ministry of Science and Education (state Contract No. 16.552.11.7008, Grant No. NSh-5602-2012.2), and the federal program "Research and Education Personnel of Innovative Russia."

*pytalev@isan.troitsk.ru

[1] G. F. Imbusch, W. M. Yen, A. L. Shawlow, G. E. Devlin, and J. P. Remeika, Phys. Rev. **136**, A481 (1964).
[2] N. Pelletier-Allard and R. Pelletier, J. Phys. C **17**, 2129 (1984).
[3] N. I. Agladze, M. N. Popova, G. N. Zhizhin, V. J. Egorov, and M. A. Petrova, Phys. Rev. Lett. **66**, 477 (1991).
[4] S. A. Klimin, D. S. Pytalev, M. N. Popova, B. Z. Malkin, M. V. Vanyunin, and S. L. Korableva, Phys. Rev. B **81**, 045113 (2010).
[5] N. I. Agladze and M. N. Popova, Solid State Comm. **55**, 1097 (1985).
[6] P. A. Tanner and M. D. Faucher, Chem. Phys. Lett. **445**, 183 (2007).
[7] V. N. Makhov, N. M. Khaidukov, D. Lo, J. C. Krupa, M. Kirm, and E. Negodin, Opt. Mater. **27**, 1131 (2005).
[8] Ch. Ma, P. A. Tanner, Sh. Xia, and M. Yin, Opt. Mater. **29**, 1620 (2007).
[9] X. Zhou, M. F. Reid, M. D. Faucher, and P. A. Tanner, J. Phys. Chem. B **110**, 14939 (2006).
[10] X. Zhou, P. A. Tanner, and M. D. Faucher, J. Phys. Chem. C **111**, 683 (2007).
[11] M. L. Falin, K. I. Gerasimov, A. M. Leushin, and N. M. Khaidukov, J. Lumin. **128**, 1103 (2008).
[12] P. A. Tanner, Ch.-K. Duan, V. N. Makhov, M. Kirm, and N. M. Khaidukov, Opt. Mater. **31**, 1729 (2009).
[13] P. A. Tanner, Ch.-K. Duan, V. N. Makhov, M. Kirm, and N. M. Khaidukov, J. Phys. Condens. Matter **21**, 395504 (2009).
[14] X. Zhou, Sh. Xia, and P. A. Tanner, J. Phys. Chem. B **111**, 8677 (2007).
[15] M. R. Roser, J. Xu, S. J. White, and L. R. Corruccini, Phys. Rev. B **45**, 12337 (1992).
[16] A. M. Stoneham, Rev. Mod. Phys. **41**, 82 (1969).
[17] W. T. Carnall, G. L. Goodman, K. Rajnak, and R. S. Rana, J. Chem. Phys. **90**, 3443 (1989).
[18] V. V. Klekovkina, A. R. Zakirov, B. Z. Malkin, and L. A. Kasatkina, J. Phys. Conf. Ser. **324**, 012036 (2011).
[19] K. W. H. Stevens, Proc. Phys. Soc. Lond. A **65**, 209 (1952).
[20] Z. I. Ivanenko and B. Z. Malkin, Fiz. Tverd. Tela (Leningrad) **14**, 153 (1972) [Sov. Phys. Solid State **14**, 122 (1972)].
[21] M. N. Popova, E. P. Chukalina, B. Z. Malkin, and S. K. Saikin, Phys. Rev. B **61**, 7421 (2000).
[22] M. A. H. McCausland and I. S. Mackenzie, Adv. Phys. **28**, 305 (1979).
[23] A. Abragam and B. Bleaney, *Electron Paramagnetic Resonance of Transition Ions* (Clarendon Press, Oxford, UK, 1970).
[24] M. A. Krivoglaz, *Theory of Scattering of X-rays and Thermal Neutrons by Real Crystals* (Nauka, Moscow, Russian Federation, 1967).
[25] A. M. Kosevich, *The Crystal Lattice* (Wiley-VCH, Weinheim, Germany, 2005).
[26] M. A. Ivanov, V. Y. Mitrofanov, L. D. Falkovskaya, and A. Y. Fishman, J. Magn. Magn. Mater. **36**, 26 (1983).
[27] B. Z. Malkin, in *Spectroscopy of Solids Containing Rare-Earth Ions*, edited by A. A. Kaplyanskii and R. M. Macfarlane (Elsevier Science Publishers, Amsterdam, the Netherlands, 1987), Chap. 2, p. 13.
[28] B. Z. Malkin, in *Spectroscopic Properties of Rare Earths in Optical Materials*, edited by G. Liu and B. Jacquier (Springer, Berlin, Germany, 2005), Chap. 3, p. 130.
[29] R. M. Sternheimer, M. Blume, and R. F. Peierls, Phys. Rev. **173**, 376 (1968).
[30] A. J. Freeman and R. E. Watson, Phys. Rev. **127**, 2058 (1962).
[31] E. Clementi and A. D. McLean, Phys. Rev. **133**, A419 (1964).
[32] R. D. Shannon, Acta Crystallogr. A **32**, 751 (1976).
[33] E. J. Veenendaal, H. B. Brom, and W. J. Huiskamp, Physica B + C **121**, 1 (1983).
[34] R. J. Elliott, R. T. Harley, W. Hayes, and S. R. P. Smith, Proc. R. Soc. Lond. A **328**, 217 (1972).